An elastoplastic constitutive model for assessing ground settlements induced by deep excavations

Hiba El-Arja, Sébastien Burlon, Emmanuel Bourgeois

Original Study **Open Access**

Hiba El-Arja, Sébastien Burlon, Emmanuel Bourgeois*

An elastoplastic constitutive model for assessing ground settlements induced by deep excavations

https://doi.org/10.2478/sgem-2023-0011
received January 16, 2023; accepted May 13, 2023.

Abstract: Ground movements induced by deep excavations may cause damages on neighboring existing buildings. Finite element simulations generally give acceptable estimates of the horizontal displacements of the retaining wall, but results are less satisfactory for the vertical displacements of the ground surface behind the structure. A possible explanation is that most constitutive models describe volumetric strains in a simplified way. This paper proposes an elastoplastic constitutive model aimed at improving the prediction of vertical displacements behind retaining walls. The model comprises a single plastic mechanism with isotropic strain hardening, but has a specific flow rule that allows to generate contractive plastic strains. Identification of the parameters based on triaxial tests is explained and illustrated by an example of calibration. A numerical analysis of a well-documented sheet pile wall in sand in Hochstetten (Germany) is presented. The results given by the model are compared with the measurements and with those obtained using the Hardening Soil Model. The potential advantages of the proposed model are then discussed.

Keywords: deep excavations, settlements, constitutive model, finite element method, elastoplastic model.

1 Introduction

The densification of urban areas implies the construction of deep excavations nearby sensitive constructions, for lack of available space at the surface. Most analyses are focused on wall displacements (Zhang *et al.*, 2015a, Goh *et al.*, 2017a), but the prediction of the displacements induced in the surrounding ground is a major challenge to avoid damages on existing buildings. Few calculation methods are able to assess not only the displacements of the retaining structure, but also the vertical displacements of the supported ground: the finite element method (FEM) makes it possible to evaluate such settlements, while taking into account a wide range of configurations and construction techniques.

However, FEM simulation results are not always consistent with observations: the removal of the weight of the excavated ground induces a heave of the bottom of the excavation and may lead to poor prediction of the settlement of the ground behind the retaining structure (Schweiger, 2002a, Coquillay *et al.*, 2005, Elmi *et al.*, 2006, Zhang *et al.*, 2018). In terms of finite element simulations, constitutive models combining a linear elastic model and a shear strength failure criterion tend to predict ground heave behind the retaining structure instead of settlement (Jardine *et al.*, 1986; Finno and Harahap, 1991; Simpson, 1992; Finno, 2008) and to overestimate the extent of the influence zone (Delattre, 2004). These two issues are fundamental in terms of design. In practice, designers take into account the limits of linear elasticity by assuming that the deformations are within a given range and then adjust deformation moduli to obtain acceptable horizontal displacements. Using nonlinear elastic models (Duncan and Chang, 1970; Jardine *et al.*, 1986; Zdravkovic *et al.*, 2005) gives very good results regarding the prediction of horizontal displacements of the retaining structures and improves the prediction of settlements behind the retaining structure. However, results for settlements can still be improved. Besides, the behavior of geomaterials is not only nonlinear, but also irreversible. It can be argued that, around deep excavations, plastic strains become prominent and must be precisely modeled to predict the settlements generated behind the retaining wall.

The choice of the yield function, the flow rule, and the hardening rule is, therefore, essential. A popular constitutive model for excavation problems is the "Hardening Soil Model" (Schanz *et al.*, 1999) and its extension HSM-small strain (Benz, 2007). It is

***Corresponding author: Emmanuel Bourgeois,** Univ Gustave Eiffel, Marne-la-Vallée, France, E-mail: emmanuel.bourgeois@univ-eiffel.fr; ORCID: 0000-0002-3505-7168
Hiba El-Arja, Univ Gustave Eiffel, Marne-la-Vallée, France
Hiba El-Arja, Sébastien Burlon, Terrasol Setec, Paris, France

an elastoplastic model with a nonlinear elasticity and two plastic strain-hardening mechanisms: a deviatoric mechanism and a volumetric mechanism. It was first implemented in Plaxis (Plaxis, 2020), and other FE software reproduce it at least partially (for instance, Zsoil [Obrzud and Truty, 2018] or CESAR-LCPC [Itech, 2021]). This model has significantly improved the assessment of ground displacements induced by excavations (Obrzud, 2010; Obrzud and Truty, 2018), but its formulation is complex, so it is not easy to anticipate the influence of some of the parameters on the results of the simulation of an excavation.

In this paper, an elastoplastic constitutive model called "the Hardening Contractive Dilatant model," or, in short, the HCD model is proposed. It aims to be easily used by engineers. First, the formulation is presented and a methodology is proposed for the determination of parameters. An application of the HCD model to the simulation of the construction of an experimental sheet pile wall in Germany is then presented.

2 Formulation of the HCD model

The HCD model is derived from a model developed for sands under monotonic and then under cyclic loading, called MODSOL (Chehade, 1991; Khoshnoudian, 2002; Khoshravan Azar, 1995; Shahrour and Ousta, 1998; Shahrour *et al.*, 1995a; Zaher, 1995).

2.1 Elastic part of the model

The proposed approach is based on the idea that the plastic part of the strain plays a major role in the behavior of deep excavations, so that the elastic part of the model does not need to be described in detail. Only two parameters, Young's modulus and Poisson's ratio, are required. Thus, the formulation of the elastic part of the HCD model is not as flexible or versatile as that of the Hardening Soil Model or the HS-small model, but it is much simpler (it is worth recalling that the elastic part of these models requires five and six parameters, respectively, in addition to the strength parameters c and φ). In other words, we advocate the idea that, for deep excavations, the elastic part of the constitutive model can be kept simple; it may not be appropriate for other types of structures, such as shallow foundations or tunnels.

Note that the finite element code CESAR, in which the HCD model is programmed, makes it possible to combine the plastic part of the HCD model with a wide range of elastic models: linear models with moduli varying with depth, nonlinear models (the nonlinear elasticity of the modified Cam-Clay model, of HSM, or the Fahey–Carter model, etc.).

2.2 Plastic regime

Regarding the plastic regime, the model aims at reproducing the main phases defined by Fern and Soga (2018) as shear strain develops: initial contractive hardening phase, phase transition point (Tatsuoka *et al.*, 1986), dilatant hardening phase, then evolution toward a regime where the volumetric plastic strain remains constant.

2.2.1 Yield function

The yield function is a function of the principal stresses and accounts for the influence of the Lode angle:

$$f(p,q,\theta) = q - R(\theta)(p + p_c) \tag{1}$$

where p denotes the mean effective stress, q the deviatoric stress, and θ the Lode angle:

$$p = \frac{1}{3}\mathrm{tr}(\bar{\bar{\sigma}}) \tag{2}$$

$$q = \sqrt{\frac{3}{2}\bar{\bar{s}}:\bar{\bar{s}}} \tag{3}$$

$$\theta = \frac{1}{3}\mathrm{Arcsin}\left(\frac{3\sqrt{3}J_3}{2J_2^{3/2}}\right) \tag{4}$$

$$\bar{\bar{s}} = \bar{\bar{\sigma}} - p\,\bar{\bar{1}} \;\; ; \;\; J_2 = \frac{1}{2}\bar{\bar{s}} : \bar{\bar{s}} = \frac{1}{2}s_{ij}s_{ij} \;\; ; \;\; J_3 = \frac{1}{3}\bar{\bar{s}}:\bar{\bar{s}}:\bar{\bar{s}} = \frac{1}{3}\,s_{ij}s_{jk}s_{ki} \tag{5}$$

It follows from equation (1) that the yield surface is a cone in the principal stress state (with a noncircular trace in the deviatoric plane, because $R(\theta)$ depends on the the Lode angle, see Figures 1 and 2). In equation (1), care must be taken that the chosen yield surface is very simple: as a consequence, p_c, which represents the distance from the apex of the yield surface to the origin of the effective principal stress space, should be interpreted as a parameter describing (together with $R(\theta)$) the shear strength, rather than the material tensile strength. Besides, p_c remains constant; by contrast, $R(\theta)$ is the local strain-hardening variable and varies as plastic strains

evolve. Its initial value $R_o(\theta)$ defines the initial opening and shape of the elastic domain and is a function of the initial friction angle φ_o and the Lode angle θ according to the equation

$$R_o(\theta) = \frac{6 \sin \varphi_0}{3 - \sin \varphi_o \sin 3\theta} \quad (6)$$

2.2.2 Hardening rule and failure surface – ultimate friction angle

As plastic strains develop, the hardening variable $R(\theta)$ evolves according to the equation

$$R(\theta) = R_o(\theta) + \left(R_f(\theta) - R_o(\theta)\right)\frac{\varepsilon_d^p}{b + \varepsilon_d^p} \quad (7)$$

with

$$R_f(\theta) = \frac{6 \sin \varphi_{ult}}{3 - \sin \varphi_{ult} \sin 3\theta} \quad (8)$$

where φ_{ult} and b are material parameters. The Lode angle θ in equations (6)–(8) allows to distinguish compression stress paths (sin 3θ=1) and extension stress paths (sin 3θ=-1).

In equation (7), we use the plastic deviatoric strain ε_d^p defined as (Shao and Desai, 2000):

$$d\varepsilon_d^p = \sqrt{\frac{2}{3} d\bar{\bar{\varepsilon}}_d^p : d\bar{\bar{\varepsilon}}_d^p} \quad (9)$$

Because ε_d^p can only increase, according to (9), the model excludes any softening behavior.

For large values of ε_d^p, the yield function tends to become

$$f_f = q - R_f(\theta)(p + p_c) \quad (10)$$

φ_{ult} is the ultimate friction angle, whereas parameter b describes the rate of strain hardening: for $\varepsilon_d^p = b$, R takes the value $(R_o+R_f)/2$ at the center of the interval between its initial value R_o and its asymptotic value R_f.

2.2.3 Flow rule – characteristic friction angle

The originality of the proposed formulation lies in the fact that the flow rule is not defined by a plastic potential. Instead, the plastic strain increment is split into a deviatoric part $d\bar{\bar{\varepsilon}}_d^p$ and a volumetric part $d\bar{\bar{\varepsilon}}_v^p$:

$$d\bar{\bar{\varepsilon}}^p = d\bar{\bar{\varepsilon}}_v^p + d\bar{\bar{\varepsilon}}_d^p = d\lambda \left[G_v(p,q) + G_d(p,q)\right] \quad (11)$$

where $d\lambda$ is the plastic multiplier and the two functions G_v and G_d define the direction of the volumetric and deviatoric strain increments, respectively:

$$G_v(p,q) = \exp\left(-\alpha_o \varepsilon_d^p\right)\left[(p + p_c) - \frac{q}{M_c(\theta)}\right]\frac{\bar{\bar{I}}}{3} \quad (12)$$

$$G_d(p,q) = \frac{(p + p_c)}{M_c(\theta)}\frac{3}{2}\frac{\bar{\bar{s}}}{q} \quad (13)$$

where the parameter $M_c(\theta)$ depends on the Lode angle according to the equation

$$M_c(\theta) = \frac{6 \sin\varphi_c}{3 - \sin\varphi_c \sin 3\theta} \quad (14)$$

which introduces an additional material parameter noted φ_c and called "characteristic angle."

Three cases can be distinguished:

- If $q<M_c(\theta)(p+p_c)$, the behavior is contractive;
- If $q=M_c(\theta)(p+p_c)$, the soil reaches the characteristic state, which corresponds to the phase transition point from a contractive to a dilatant behavior; and
- If $q>M_c(\theta)(p+p_c)$, the behavior is dilatant.

The proposed flow rule makes it possible to better represent the volumetric strains at the onset of the plastic regime because contractive plastic strain compensates for the dilatant volumetric elastic strains.

The transition between contractive and dilative regimes for the volumetric strain is similar to Rowe's Stress dilatancy equation (Rowe, 1962), which can be adapted to express the mobilized dilatancy angle as (Schanz and Vermeer, 1996):

$$\sin \psi_m = \frac{\sin \varphi_m - \sin \varphi_{cv}}{1 - \sin \varphi_m \sin \varphi_{cv}} \quad (15)$$

But in the formulation of the HCD model, the plastic strain is not described by a plastic potential and a dilatancy angle: instead, equations (12) and (13) describe independently the deviatoric and the volumetric part of the plastic strain increment. Equation (12) shows that, for large deviatoric plastic strains, the volumetric plastic strain increment tends toward zero. Besides, the parameter α_o makes it possible to control the rate at which plastic volumetric strain rate tends toward zero as the deviatoric plastic strain ε_d^p increases. Note that the volumetric plastic strain increment is not related to a critical state defined by the stress ratio, for instance, in contrast to the approach proposed by Roscoe *et al.* (1958) or Schofield and Worth (1968).

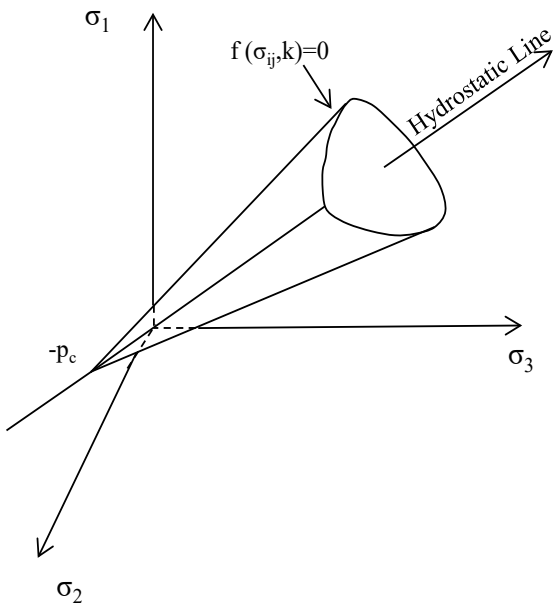

Figure 1: Yield surface in the principal stress space.

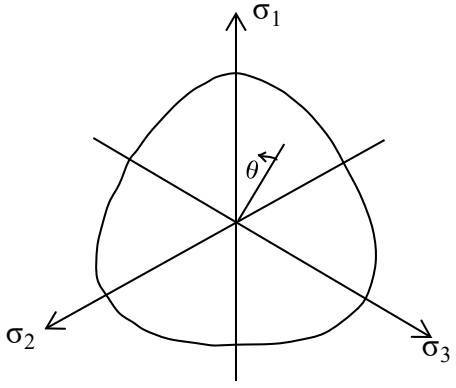

Figure 2: Section of the yield surface in the deviatoric plane.

2.3 Example of calibration of the HCD model on triaxial tests

A clear methodology for the determination of the model parameters based on data available for a real project is a crucial issue in practice. The formulation of the HCD model includes eight parameters:

- the elastic parameters: Young's modulus E and Poisson's ratio ν;
- the initial friction angle φ_o, the apex parameter p_c and the ultimate friction angle φ_{ult}; and
- the characteristic angle φ_o and the hardening parameters α_o and b.

Table 1: Summary of the triaxial tests considered in this study.

Test	Depth	Type of soil	Type of test
B	6.5–7	Very fine silty sand	Consolidated drained CD
C	8.5–9.5	Slightly sandy pebbles and gravel	Consolidated drained CD
E	13.7–14	Silty clay	Consolidated drained CD

In this paragraph, the calibration of the model parameters is discussed using triaxial tests carried out for a metro station of line 15 south of the "Grand Paris Express" project. The data were provided by Soletanche-Bachy (a French deep foundations contractor). Tests with different confining stresses have been performed on samples from three layers (Table 1).

In a first step, the apex parameter p_c and the ultimate friction angle φ_{ult} can be deduced from the stresses at failure in the drained triaxial tests.

As a first approximation, it is assumed that the elastic limit corresponds to an axial strain of 0.1%, which makes it possible to calculate Young's modulus E and Poisson's ratio ν. Denoting the mean effective stress and the deviatoric stress for this value of the axial strain as p_0 and q_0, parameter R_o is obtained from the equation (1):

$$R_o = \frac{q_o}{p_o + p_c} \tag{16}$$

Angle φ_o can then be estimated using equation (6) with 3θ=1:

$$\varphi_o = \text{Arcsin}\frac{3R_o}{6 + R_o} \tag{17}$$

The characteristic angle φ_c corresponds to the transition between the contractive and the dilatant behavior and its value can be determined by adjusting the axial strain ε_a–volumetric strain ε_v curve. The value of parameter b is determined by fitting the simulations on the axial strain ε_a–deviatoric stress q curve.

Eventually, the value of parameter α_o is obtained by fitting the end of the simulated axial strain–volumetric strain curve on the results of the drained triaxial tests.

Table 2 summarizes the parameters obtained for each test. Numerical results are shown in Figures 3–5 and compared with test results. Note that, for tests E1, E2 and E3, the measured deviatoric stress presents a peak value and then a progressive decrease: as explained before, such a behavior cannot be reproduced using the HCD model.

Table 2: Parameters of the HCD model for tests B, C, and E (σ_c denotes the confining pressure).

		σ_c	E	v	φ_o	p_c	φ_{ult}	α_o	φ_c	b
		kPa	MPa	-	°	kPa	°	-	°	-
Test B	1	150	45	0.2	7	10	35	1	31	0.005
	2	250	70	0.2	7	10	35	1	32	0.008
	3	400	107	0.2	7	10	35	1	33	0.009
Test C	2	200	133	0.1	15	15	41	1	38	0.002
	3	350	233	0.127	15	15	41	1	39	0.005
Test E	1	200	16	0.12	1.2	60	23	1	20	0.004
	2	350	45	0.12	2.2	60	23	1	20	0.005
	3	550	112	0.14	4.2	60	23	1	21	0.015

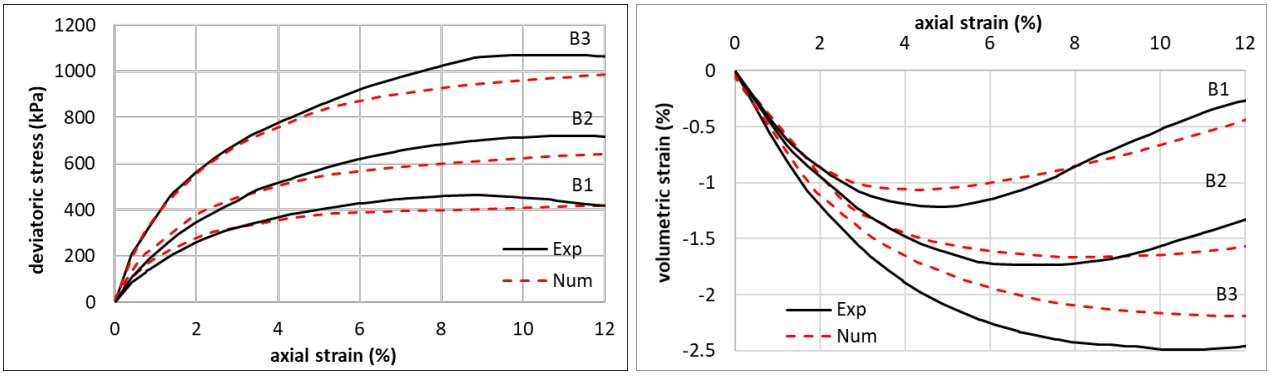

Figure 3: Calibration of the HCD model on tests B1, B2, and B3.

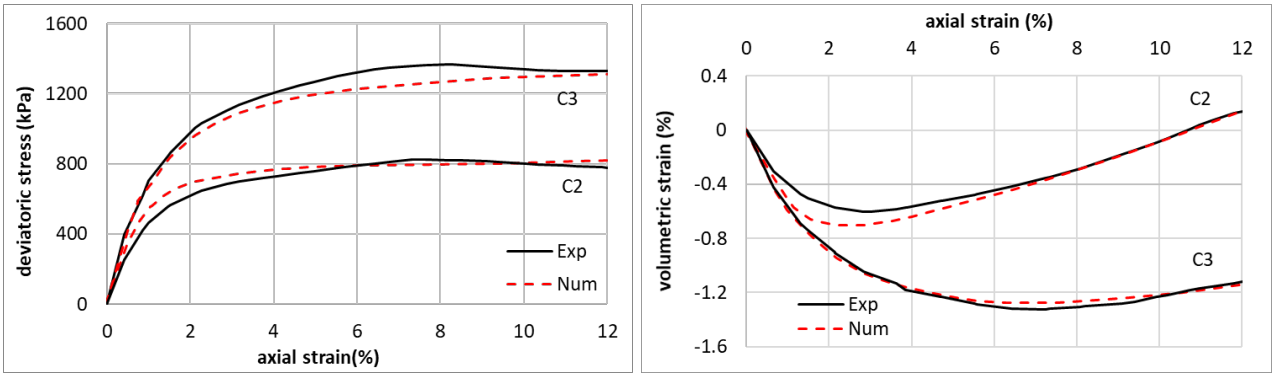

Figure 4: Calibration of the HCD model on tests C2 and C3.

Besides, the results presented in Table 2 show the fitting of the parameters for each test: this leads to different values of Young's modulus for the different confining pressures. To overcome this difficulty, one can choose an average value or use a modulus value varying with the depth. This is the choice adopted in Section 3.

Two additional drained triaxial tests are performed on an alluvial soil: a monotonic test and a test with two loading–unloading cycles. In the latter case, the shear stress increases until the axial strain reaches 0.5%, then it returns to zero, then it increases up to 1.5% axial strain; a second unloading occurs followed by a final loading up to 15% axial strain.

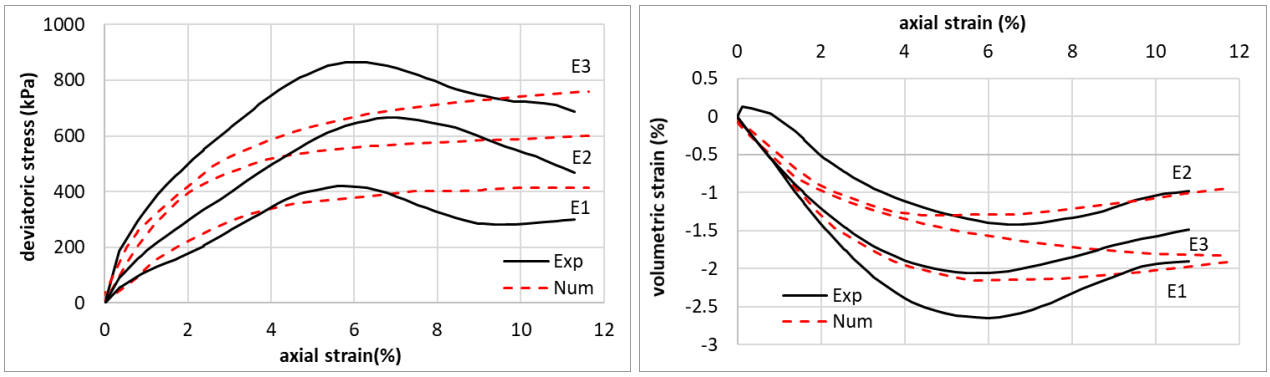

Figure 5: Calibration of the HCD model on tests E1, E2, and E3.

Table 3: HCD model parameters.

	E	ν	φ_o	p_c	φ_{ult}	α_o	φ_c	b
	MPa		°	kPa	deg		deg	
Monotonic test (confining pressure 175 kPa)	57	0.4	φ_{min}	0	37	8	27	0.001
Cyclic test (confining pressure 157 kPa)	57	0.4	φ_{min}	0	37	20	31	0.003

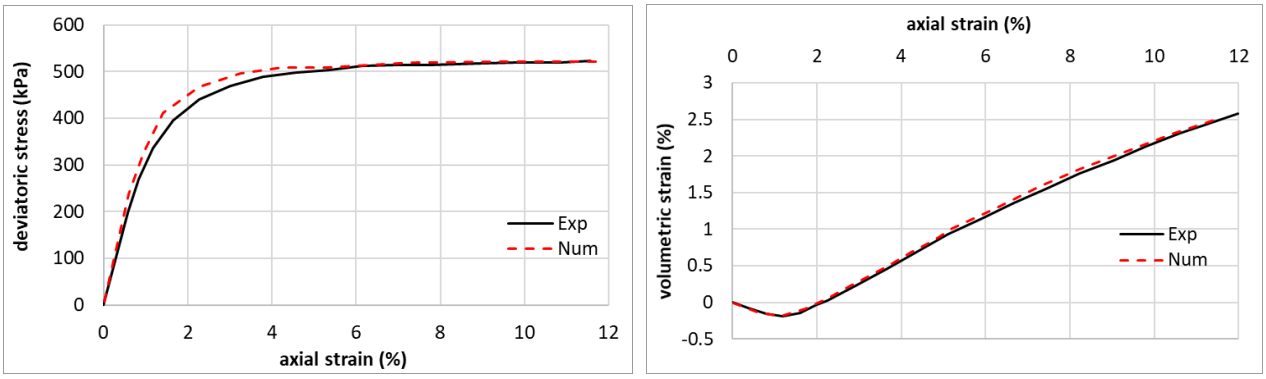

Figure 6: Calibration of the HCD model on the monotonic drained triaxial test on alluvial material.

The slope of the axial strain–deviatoric stress curves at the beginning of the monotonic test and on the unloading cycles is chosen to define the value of Young's modulus E. Poisson's ratio ν is determined using the slopes of the volumetric strain–axial strain curves at the beginning of the monotonic test and on the unloading cycles. Ultimate shear strength parameters are determined in the p-q plane for the highest levels of strain. Parameter φ_o is determined by assuming that the initial stress state of the triaxial test is on the boundary of the elastic domain. Parameters of the flow rule α_o and φ_c are obtained by fitting the volumetric strain–axial strain curve on the experimental results. Parameter b, which governs the strain-hardening mechanism, is fitted to reproduce the deviatoric stress–axial strain curves.

Table 3 and Figures 6 and 7 show the results of the calibration.

This example of calibration shows that the HCD model has the ability (or the flexibility) to reproduce accurately the results of triaxial tests and proposes to determine the values of the parameters in a given order. It remains to discuss the ability of the model to reproduce the behavior of a full-scale structure.

3 Case history: Hochstetten sheet pile wall

This section presents a numerical analysis of an experiment carried out in Hochstetten, Germany, by the

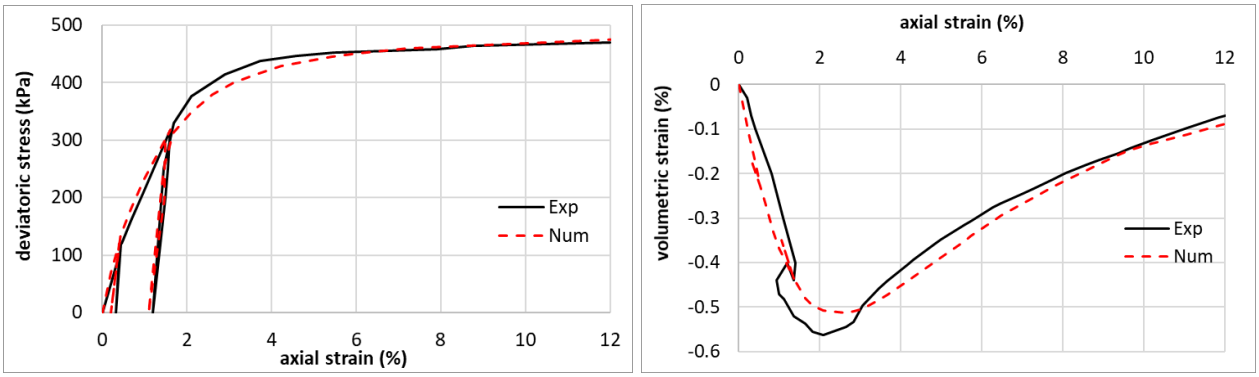

Figure 7: Calibration of the HCD model on the drained triaxial test with unloading cycles on alluvial material.

University of Karlsruhe (von Wolfferdorff 1994a, 1994b). A sheet pile wall was monitored during several construction and loading stages. The experiment was the basis for a prediction exercise: 18 contributions were submitted using finite element models and 23 using the subgrade reaction coefficient method. Shahrour *et al.* (1995b) and Coquillay (2005) noted that the overall behavior and the horizontal displacements obtained by numerical simulations were reasonably close to the measures, but reproducing the settlements behind the wall remained a challenge.

In the following sections, we present finite element calculations for this sheet pile wall performed using the finite element software CESAR-LCPC in which the HCD model has been implemented.

3.1 Description of the experiment

The Hochstetten sheet pile wall was made of sheet piles vibrodriven down to a depth of 6 m in a sandy ground (see Figure 8). The water table was located 5.5 m below the natural ground level. The experiment includes the following stages:

0) Installation of the sheet piles
1) Excavation down to a depth of 1.75 m
2) Installation of three struts at a depth of 1.25 m with a spacing of 2.4 m and a prestressing force of 10 kN per strut
3) 4) 5) Excavations down to 3, 4, 5 m
6) Application of a 10 kPa pressure at the ground surface between 1 and 5 m from the wall (by means of a basin filled with water)

After the application of the surface load, the struts were progressively shortened. This phase is not taken into account hereafter.

The monitoring devices measured bending moments in the wall, forces in the struts, horizontal displacements of the wall, vertical displacements of the ground surface behind the wall, and earth pressure on both sides of the wall. Results of the experiment have been made public by von Wolffersdorff (1994b) and reproduced by Shahrour *et al.* (1995) and Coquillay (2005).

Case studies of monitored full-scale structures are always extremely valuable for the validation of numerical simulations, but this experiment is especially interesting because the structure, the hydraulic regime, and the lithology of the site are simple. Notably, the fact that the sand is relatively homogeneous avoids the addition of uncertainties attached to the determination of the parameters for several layers. Moreover, the experiment was carried out in well-controlled conditions, which limits uncertainties that are frequent in actual construction sites, such as undocumented transient phases (temporary storage of excavated material, for instance). Besides, the monitoring devices provide rich information, unlike many references in the literature for which it is difficult to precisely reconstruct both the settlement measurements behind the retaining structures and the geotechnical context.

3.2 Geometry, mesh, and modeling assumptions

The main assumptions are the following:

– The wall is modeled in plane strain conditions. The excavation is 4 m wide and not symmetric: the struts are connected to another stiffer wall. The lateral extension of the calculation model is equal to 50 m and the vertical extension is equal to 15 m; the mesh, shown in Figure 9, comprises 1200 quadratic elements and 3700 nodes.

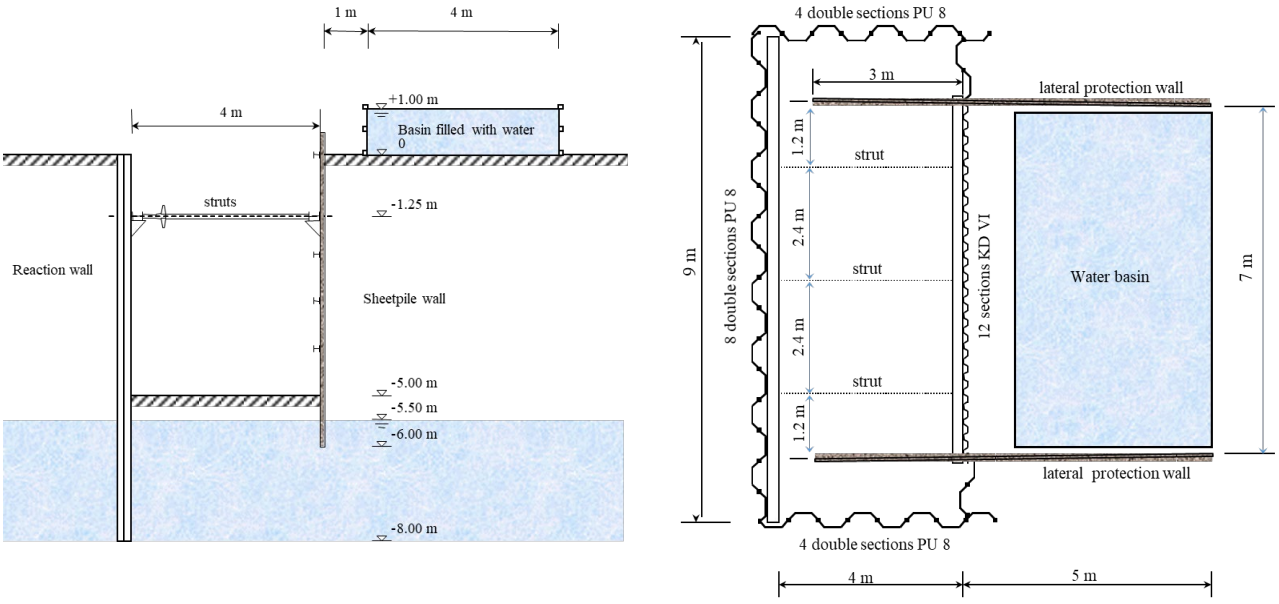

Figure 8: Experimental setup (a) front view, (b) top view.

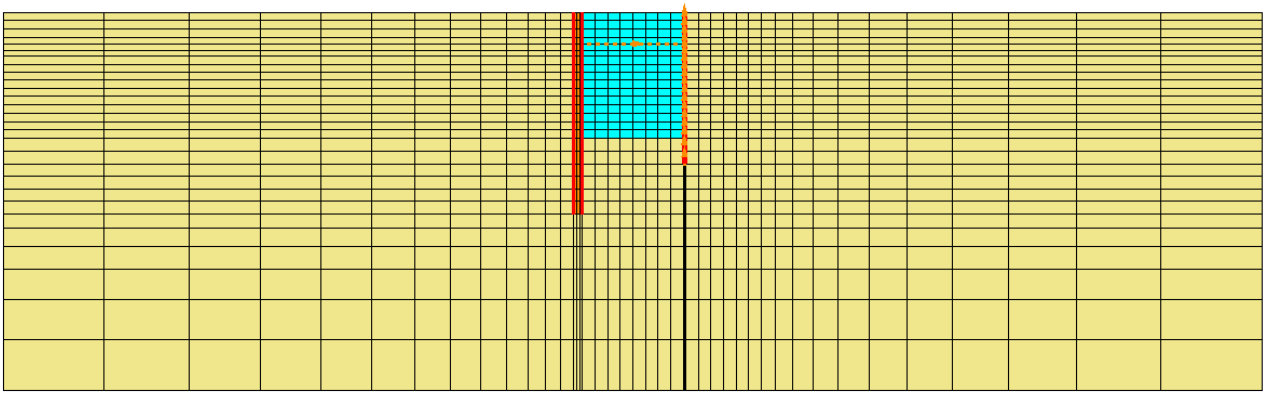

Figure 9: Mesh used for the simulations.

- The walls are modeled using surface elements (as opposed to beam elements) and the row of struts is modeled using a simple "bar" element acting as a horizontal spring; in other words, the bending stiffness of the struts is neglected.
- The installation stage is not modeled; the so-called "wished-in-place" method is used.
- Interface elements are introduced between the wall and the ground.
- The analysis is carried out in drained condition.

The calculation comprises a sequence of six stages that match the description of the experiment given in Section 3.1.

3.3 Boundary conditions

The horizontal and vertical displacements are set to zero on the mesh lower boundary, and the horizontal displacement is zero on the left and right boundaries.

3.4 Initial stresses

The initial stresses are geostatic:

$$\sigma_v' = \gamma z\,;\ \sigma_h' = K_o\,\gamma z \tag{18}$$

Table 4: Parameters of the reaction wall and the sheet pile wall.

Wall	E (MPa)	I (cm^4/m)	A (cm^2/m)	E_{eq} (MPa)	t_{eq} (cm)
Reaction wall	210,000	968	106	24,400	10
Sheet pile wall	210,000	11,610	116	6800	35

where the earth pressure coefficient K_o is chosen equal to 0.318 (which corresponds to K_o=1-sinφ with a friction angle φ of 43°, see Section 3.7) the value of the (dry) sand volumetric weight is taken equal to 17 kN/m^3.

3.5 Properties of the walls and struts

The axial stiffness *EA* and the flexural stiffness *EI* (per unit length of wall) are known for the experimental sheet pile wall and for the reaction wall. Following Coquillay (2005), in the plane strain simulations, an "equivalent" thickness t_{eq} and an equivalent Young's modulus E_{eq} are used, so that the following conditions are fulfilled:

$$E_{eq}\, t_{eq} = EA\,;\, E_{eq}\, t_{eq}^3/12 = EI$$

The parameters are summarized in Table 4 (thicknesses being rounded to whole numbers in cm).

The row of struts is modeled by a two-node linear element withstanding only tension/compression forces, with a linear elastic behavior; the elastic parameters are deduced from the axial stiffness of the struts and the spacing. In the simulations presented hereafter, we adopt the values reported in Coquillay (2005): E = 210,000 MPa and A = 0.02 m^2/m. At the installation (stage 2), a prestressing force of 4.2 kN/m is taken into account, corresponding to the force in each strut (10 kN) divided by the spacing between struts (2.4 m).

3.6 Interface model and parameters

For the simulations with both models (HSM and HCD), the interface between the walls and the sand is modeled by zero-thickness elements called "joint elements," based on the approach proposed by Goodman *et al.* (1968), characterized by their cohesion c_{int} and friction angle φ_{int}. It is often suggested that these parameters can be deduced from the cohesion and friction angle c_{sand} and φ_{sand} of the sand by $c_{int} = R_{\text{inter}} \tan c_{sand}$ and $\tan \varphi_{int} = R_{\text{inter}} \tan \varphi_{sand}$, where R_{inter} is a coefficient that remains to be discussed. By contrast, in the following, the interface strength properties are set independently from those of the sand. Since no specific data was available, after preliminary parametric studies, the following values are selected:

$$c_{int} = 1 \text{ kPa and } \varphi_{int} = 5°$$

A short discussion regarding the influence of this choice is presented in Section 4.

3.7 Sand parameters

The files of the prediction exercise contained the results of triaxial tests carried out on the sand of the site. The results of three monotonic drained tests are reproduced in Coquillay (2005), under the names S5DK15, S5DK21, and S5DK31 for confining pressures of 100, 200, and 300 kPa, respectively.

We have performed a calibration of the parameters of two models: the Hardening Soil Model (Schanz *et al.*, 1999), because it is very widely used by engineering companies or firms and has become a standard, and the HCD model.

The calibration aimed at reproducing as much as possible the three tests considered with the same parameters. The calibration led to the parameters given in Table 5. The result of the calibration is illustrated in Figure 10 for the Hardening Soil Model and in Figure 11 for the HCD model.

For the HSM parameters, we have adopted the choices commonly adopted in engineering practice: Poisson's ratio equal to 0.1; reference stress equal to 100 kPa; E_{ur}=3E_{50}, R_f=0.9. It can be kept in mind for the following discussion that, with the proposed parameters, the simulation slightly overestimates the stiffness for the test with 100 kPa confining pressure; but, in a general way, both models reproduce the test results reasonably well, with the volumetric strain being relatively less well approximated.

Table 5: Reference parameters (calibrated on the triaxial tests) for the Hochstetten sand.

HSM	E_{ur}^{ref}=63 MPa,E_{50}^{ref}=21 MPa,ν =0.1,m=0.5, p^{ref}=100 kPa, c=5 kPa, φ =43°, ψ =14°, R_f=0.9
HCD model	E=75 MPa, ν=0.3, R_o=0, p_c=2 kPa, φ_{ult}=43°, φ_c=29°, α_o=3, b=0.0025

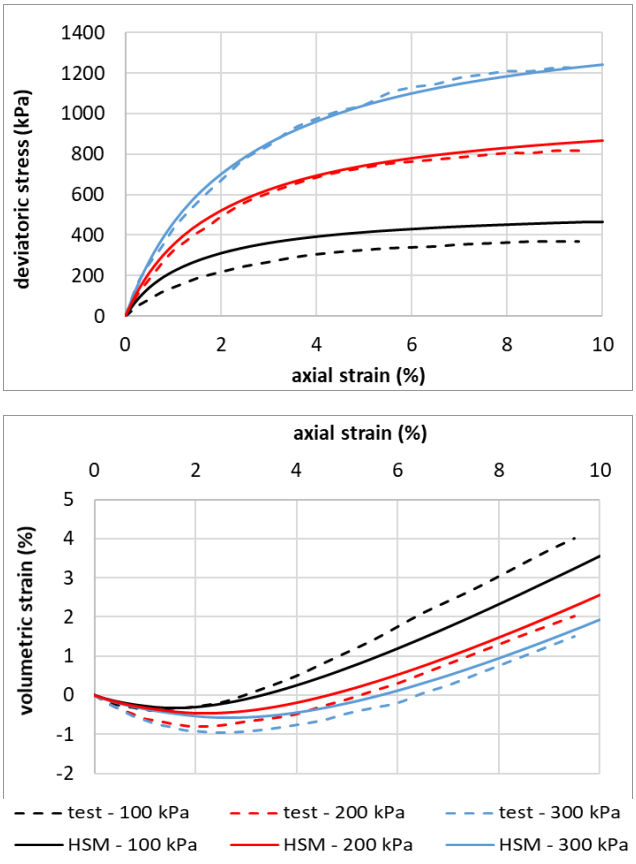

Figure 10: Results of the calibration of the Hardening Soil Model parameters.

3.8 Results

3.8.1 Results obtained with HSM

Table 6 shows the values of the maximum horizontal displacement of the sheet pile wall for the last three stages of the simulation: excavation down to 4 m, then 5 m, and application of a 10 kPa surcharge behind the wall, and of the settlement of the ground at 1 m behind the wall for the last two stages.

With the values of the reference parameters resulting from the calibration, the horizontal displacement of the wall is significantly overestimated for the last two stages, and the settlement behind the wall is also overestimated (Table 6 shows the values of the computed displacements in mm and the relative error with the measured values), in spite of the fact that the calibration of the parameters tended to overestimate the sand initial stiffness, as mentioned in Section 3.7.

With the initial estimate of the maximum horizontal displacement and of the maximum settlement in the final state being much too large, increasing the sand stiffness is a straightforward way to improve the results, without modification of other parameters. No systematic calibration procedure has been used for the model parameters, such as the ones proposed by Zhang *et al.* (2015b) or Moussaoui *et al.* (2022). The difference between simulations and measurements is simply reduced by increasing the values of the elastic moduli. The values E_{ur}^{ref}=135 MPa and E_{50}^{ref}=45 MPa are selected (instead of 63 MPa and 21 MPa, respectively; with no modification of the ratio $E_{ur}^{ref}/E_{50}^{ref}$). Table 6 shows that the adjusted moduli improve the estimated maximal horizontal displacement of the sheet pile wall at the final stage (relative error of 4%) and the settlement 1 m behind the wall at the same stage (relative error of 17%), but, of course, the simulation of the triaxial tests gives results that are less close to the laboratory data.

3.8.2 Results obtained with the HCD model

Table 7 shows the same comparisons for the HCD model. Again, we present the results with the parameters obtained by the calibration presented in Section 3.7. The results are clearly closer to the measures than those obtained with HSM for the reference parameters.

We have also adjusted the model parameters to reduce the difference with the measured values. The proposed adjustment consists in letting Young's modulus vary with the depth z according to (z)=27+5z, where E is in MPa and z is in m. With this adjustment, the model reproduces reasonably well the experimental results.

3.8.3 Comparisons HSM/HCD

This section presents a more direct comparison of the results obtained with the two models and the experimental values. Results shown below correspond to the adjusted parameters of both models.

Figure 12 compares the horizontal displacements of the wall: the simulations with the HCD model give values of the maximum displacement and of the toe displacement closer to the measures than the simulations with HSM. On

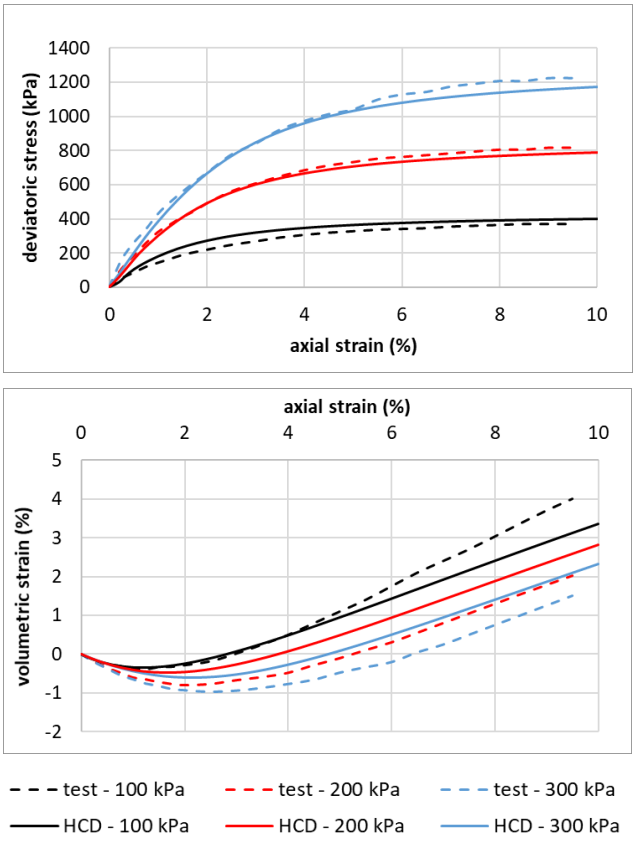

Figure 11: Results of the calibration of the HCD model parameters.

Table 6: Results obtained with HSM (displacements in mm).

	Measures	HSM (ref.)	HSM (adj.)
Max horizontal displacement – 4 m	1.83	1.34 (-27%)	0.91 (-50%)
Max horizontal displacement – 5 m	2.95	4.49 (+52%)	2.56 (-13%)
Max horizontal displacement –surcharge	3.36	5.80 (+73%)	3.28 (-2%)
Settlement 1 m behind the wall – 5 m	2.17	1.21 (-44%)	0.80 (-63%)
Settlement 1 m behind the wall – surcharge	2.80	4.18 (+49%)	2.26 (-19%)

the other hand, the horizontal displacement in the upper part of the wall is better reproduced using HSM.

Figure 13 compares the vertical displacements of the ground surface behind the wall for distances between 1 and 5 m: both models give similar results and close to the measured values. It can be estimated that the HCD model gives values rather closer to the measurements for the excavation down to 5 m.

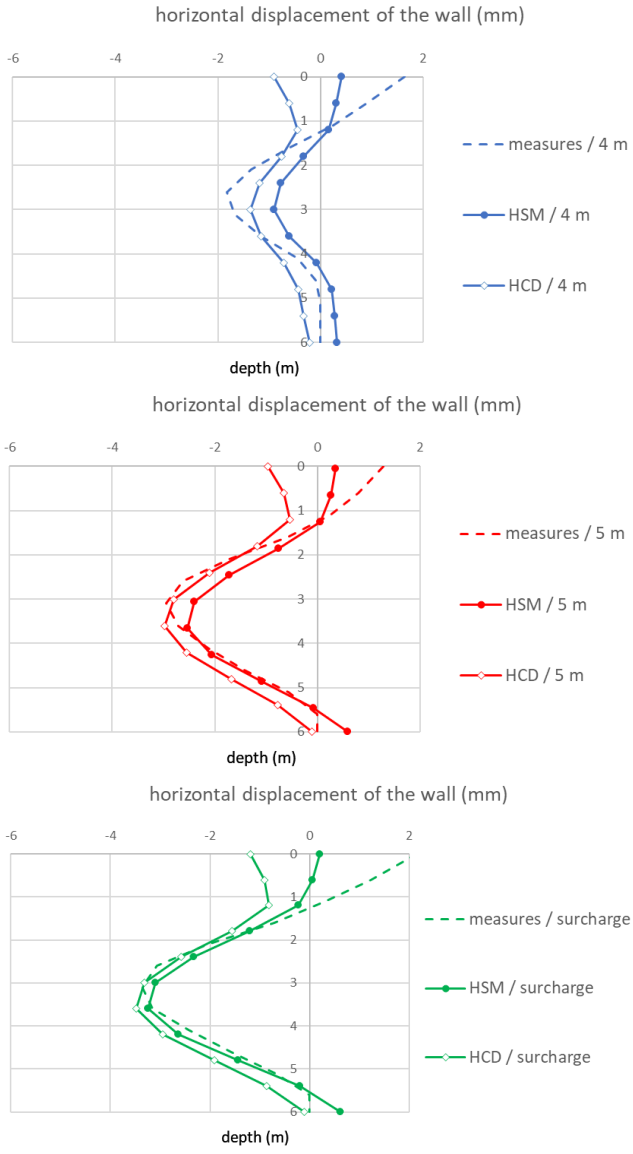

Figure 12: Comparison of the horizontal displacements (last three stages).

The results of the experiment also presented the bending moments in the sheet pile wall. The comparison between models and measures is not shown here for brevity, but confirms a strong consistency between models and experiment.

In the last place, we can compare the values of the forces in the struts for the different stages of the experiment (Figure 14). Both models give very similar results and tend to overestimate the normal forces in the struts for the last two stages.

Table 7: Results obtained with the HCD model (displacements in mm).

	Measures	HCD (ref.)	HCD (adj.)
Max. horizontal displacement – 4 m	1.83	0.86 (-53%)	1.37 (-25%)
Max. horizontal displacement – 5 m	2.95	2.53 (-14%)	2.99 (+1%)
Max. horizontal displacement – surcharge	3.36	2.86 (-14%)	3.51 (+4%)
Settlement 1 m behind the wall – 5 m	2.17	1.81 (-17%)	1.81 (-17%)
Settlement 1 m behind the wall – surcharge	2.80	2.65 (-5%)	3.04 (+8%)

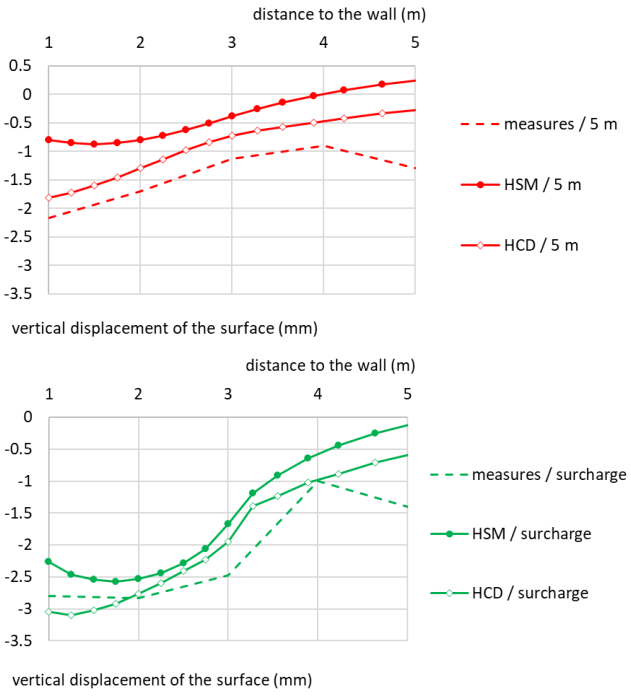

Figure 13: Comparison of the settlements behind the wall (last two stages).

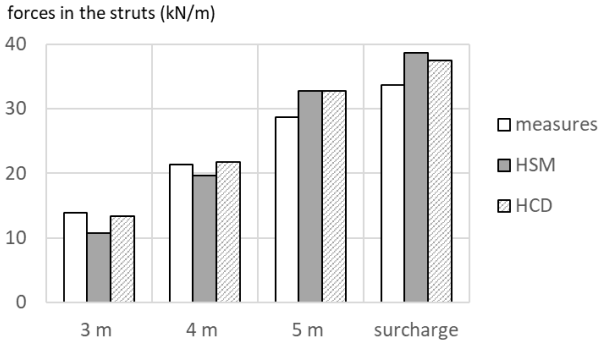

Figure 14: Comparison of the forces in the struts (for four stages: excavation down to 3, 4, and 5 m, and surcharge).

4 Discussion

Several factors may be responsible for the differences observed in the horizontal displacement of the upper part of the wall, which are as follows:

- The sheet piles were vibrodriven; for that type of installation, one can question the assumption that the stress state in the sand remains geostatic.
- Regarding the calibration on the triaxial tests, the determination of the cohesion c for the HSM model and of p_c for the HCD model is not very precise, which is an issue because a sensitivity analysis (not presented here) shows that their influence on the results is not negligible.
- The parameters of the sand–sheet pile wall interface have not been discussed in detail, yet they can also have a strong influence on the wall behavior. To illustrate this point, we have rerun the simulations with φ_{int} = 20° instead of 5° (the value of 20° is found in the analyses of the same sheet pile wall presented by Mestat and Arafati (1998), Coquillay *et al.* (2005), and Elmi *et al.* (2006), focusing on the horizontal displacements and giving poor results in terms of vertical displacements behind the wall). For both the HSM and HCD models, the maximum horizontal displacement is reduced by approximately 10% for all stages. The forces in the struts are reduced, very similar for both models, and slightly underestimated at the initial stages and close to the measurements at the surcharge step. Vertical displacements behind the wall are presented in Figure 15. The agreement with the measured settlements is less satisfactory: notably, for the excavation down to 5 m, the maximum settlement is 0.5 mm for the HSM model and 1 mm for the HCD model, while the measures give 2.2 mm. This led us to retain the value of 5° in Section 3.

Nevertheless, from a qualitative point of view, the HCD model gives good results for the simulation of the Hochstetten pile wall and, for the special case discussed here, gives better results with the parameters resulting directly from the calibration on triaxial tests as HSM. HSM performs very well too, but it was necessary to adjust the parameters derived from the calibration on the triaxial tests. It must also be kept in mind that the absolute displacements measured on the sheet pile wall were small, so a small deviation between the computed and measured values results in apparently large relative errors.

In the last place, it can be mentioned that the HCD model has also been used to perform simulations for a 30-m deep excavation in Berlin sand, with horizontal

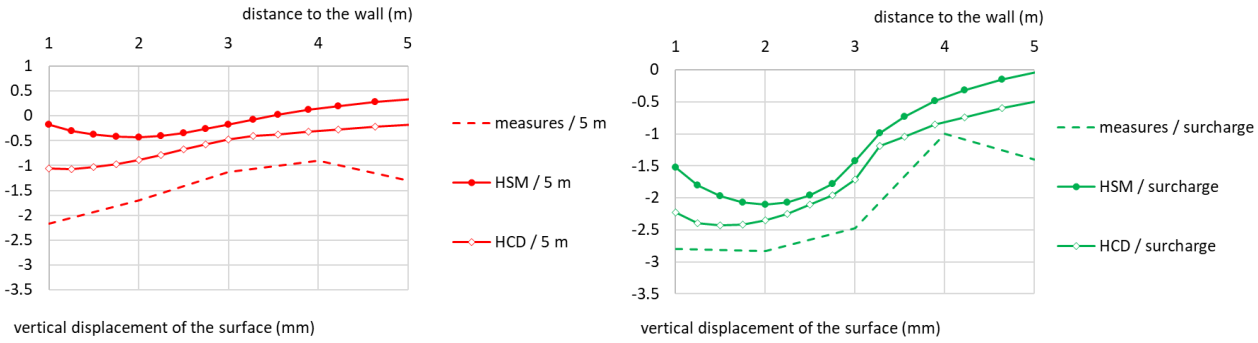

Figure 15: Comparison of the settlements behind the wall (last two stages) with a friction angle of 20° for the sand–wall interface.

displacements in the order of 30 mm. This case is well documented (Schweiger, 2002b) and often used to validate or calibrate numerical models; the results obtained with the HCD model have been presented in detail in El Arja (2020) and summarized in El Arja *et al.* (2019). The conclusions regarding the proximity between the HSM and HCD models are similar, but the comparison is less complete, since vertical displacements behind the wall had not been measured. Also, it can be noted that no attempt has been made yet to model deep excavation in clays with the HCD model or to analyze the effect of groundwater drawdown (Zhang *et al.*, 2018a, 2018b).

5 Conclusion

This paper presents a simple elastoplastic constitutive model developed to improve the prediction of the vertical displacements behind retaining walls.

One of the advantages of the HCD model is its simplicity: it involves only one plastic mechanism, and the elastic part of the model is linear and elastic. The yield surface is relatively classic and the hardening is isotropic. The originality of the model lies in the formulation of the flow rule that allows accounting for a contractive–dilatant behavior in the plastic regime.

Among the eight parameters, four are familiar (Young's modulus, Poisson's ratio, tensile strength, and friction angle); one defines the initial position of the yield surface and the last three are clearly associated with the characteristic state, the gradual decrease in plastic volumetric strain, and the rate at which the yield surface evolves toward the failure surface. Identification of the parameters based on triaxial tests is explained, and an example of calibration is presented.

For the numerical analysis of the experimental sheet pile wall of Hochstetten, the HCD model gives results that are rather closer to the measured values than HSM. It can be argued that the nonassociated flow rule of the HCD model allows to better control the volumetric plastic strains; at least, the influence of the model parameters is easy to anticipate, which facilitates the recalibration of a numerical simulation on experimental results.

Acknowledgments

The authors are grateful to Soletanche-Bachy for the results of triaxial tests carried out for the metro station of line 15 south of the "Grand Paris Express" project, to calibrate the HCD model.

References

[1] Benz, T. (2007). Small strain stiffness of soils and its numerical consequences, PhD Thesis, Universität Stuttgart.

[2] Chehade, W. (1991). Méthodologie pour la validation des modèles des géomatériaux-Application aux modèles élastoplastiques, PhD Thesis, Univ Sciences et Technologies de Lille (in French).

[3] Coquillay, S. (2005) Prise en compte de la non linéarité du comportement des sols soumis à de petites déformations pour le calcul des ouvrages géotechniques, PhD Thesis, Ecole Nationale des Ponts et Chaussées (in French).

[4] Coquillay, S., Bourgeois, E., and Mestat, Ph. (2005) A non-linear elastic-perfectly plastic model for the simulation of the Hochstetten sheet pile wall. 11th International Conference of IACMAG, Turin, Italy, June 19-24, 2005.

[5] Delattre, L. (2004). A century of retaining wall computation methods III: Modeling of retaining walls by means of the finite element method, Bull Lab Ponts et Chaussées, n°252-253, 95-117, www.ifsttar.fr/collections/BLPCpdfs/blpc_252-253_95-117_en.pdf .

[6] Duncan, J.M., and Chang, C.-Y. (1970). Nonlinear Analysis of Stress and Strain in Soils. Journal of the Soil Mechanics and Foundations Division 96, 1629–1653.

[7] El Arja, H. (2020). Contribution à la modélisation numérique des excavations profondes, PhD Thesis, Université Paris-Est.
[8] El Arja, H., Bourgeois, E., and Burlon, S. (2019). Prise en compte du mécanisme des déformations plastiques dans les calculs des excavations profondes. Proc XVII ECSMGE-2019, Reykjavik.
[9] Elmi, F., Bourgeois, E., Pouya, A., and Rospars, C. (2006) Elastoplastic Joint Element for the Finite Element Analysis of the Hochstetten Sheet Pile Wall, in Numerical methods in geotechnical engineering NUMGE 2006, Schweiger (ed), Graz, Austria, 411–416
[10] Fern, E.J., and Soga, K. (2018). The dilatancy conditions at critical state and its implications on constitutive modelling, Numerical Methods in Geotechnical Engineering NUMGE 2018, Porto, 8 p.
[11] Finno, R.J. (2008). General Report: Analysis and Numerical Modeling of Deep Excavations, Proc 6th Int Symp on Geotechnical Aspects of Underground Construction in Soft Ground, Shanghai, China, Ng, Nuang and Liu, eds., Taylor & Francis, 87-97.
[12] Finno, R.J., and Harahap, I.S. (1991). Finite Element Analyses of HDR-4 Excavation. Journal of Geotechnical Engineering 117, 1590–1609.
[13] Goh, A.T.C., Zhang, F., Zhang, W., Zhang, Y., and Liu, H. (2017a) A simple estimation model for 3D braced excavation wall deflection, Computers and Geotechnics 83, 106-113. http://dx.doi.org/10.1016/j.compgeo.2016.10.022
[14] Goh, A.T.C., Zhang, F., Zhang, W., and Chew, O.Y.S. (2017b) Assessment of strut forces for braced excavation in clays from numerical analysis and field measurements, Computers and Geotechnics 86, 141-149. http://dx.doi.org/10.1016/j.compgeo.2017.01.012
[15] Goodman, R. E., Taylor, R. L., and Brekke, T. L. (1968). A model for the mechanics of jointed rock. Journal of the Soil Mechanics and Foundations Division ASCE, Vol.94, No. SM3, 637–659.
[16] Itech (2021) General overview - Geotechnical analysis - v2021 (https://www.cesar-lcpc.com/documents/CESAR-FC-2021-EN.pdf)
[17] Jardine, R.J., Potts, D.M., Fourie, A.B., and Burland, J.B. (1986). Studies of the influence of non-linear stress–strain characteristics in soil–structure interaction. Géotechnique 36(3), 377–396 (https://doi.org/10.1680/geot.1986.36.3.377).
[18] Khoshnoudian, F. (2002). Numerical Analysis of the Seismic Behavior of Tunnels Constructed in Liquefiable Soils, Soils and Foundations, 42(6), 1–8.
[19] Khoshravan Azar, A. (1995). Problèmes de sols saturés sous chargement dynamique: modèle cyclique pour les sols et validation sur des essais en centrifugeuse, PhD Thesis, Univ Sciences et Technologies de Lille (in French).
[20] Mestat, Ph., and Arafati, N. (1998) Finite element modelling of the performance of the experimental sheet pile at Hochstetten, Bulletin de Liaison des Laboratoires des Ponts et Chaussées, 216, 19-39.
[21] Moussaoui, M., Rehab Bekkouche, S., Kamouche, H., Benayoun, F., and Goudjil, K. (2022) Identification of Soil Mechanical Parameters by Inverse Analysis Using Stochastic Methods, SSP-Journal of Civil Engineering, 17(1), DOI: 10.2478/sspjce-2022-0018
[22] Obrzud, R.F. (2010). On the use of the Hardening Soil Small Strain model in geotechnical practice, Numerics in Geotechnics and Structures, 15-42.
[23] Obrzud, R.F., and Truty, A. (2018). The Hardening soil model - A practical guidebook, Z Soil.PC 100701 report.
[24] Plaxis (2020). Material Models Manual.
[25] Roscoe, K.H., Schofield, A.N., and Wroth, C.P. (1958). On the Yielding of Soils, Géotechnique 8(1), 22–53 (https://doi.org/10.1680/geot.1958.8.1.22).
[26] Rowe, P.W. (1962) The stress-dilatancy relation for static equilibrium of an assembly of particles in contact. Proc. Royal Society of London, Mathematical and Physical Sciences, Vol. 269, Series A, 500-557.
[27] Schanz, T., and Vermeer, P. (1996) Angles of friction and dilatancy of sand, Géotechnique 46 (1), 145-151.
[28] Schanz, T., Vermeer, P.A., and Bonnier, P.G. (1999). The hardening soil model: Formulation and verification, Beyond 2000 in Computational Geotechnics, R.B.J. Brinkgreve, ed. , 281–296.
[29] Schofield, A., and Worth, P. (1968). Critical State Soil Mechanics, Mc Graw-Hill.
[30] Schweiger, H.F. (2002a). Benchmarking in Geotechnics_Part I: Results of benchmarking. Technical report CGG IR006 2002, Institute for Soil Mechanics and Foundation Engineering, Graz University of Technology.
[31] Schweiger, H.F. (2002b). Results from numerical benchmark exercises in geotechnics, 5th Conf on Num Meth in Geotechnical Engineering NUMGE 2002, Mestat (ed), Paris, volume 1, 305–314.
[32] Shahrour, I., and Ousta, R. (1998). Numerical analysis of the behavior of piles in saturated soils under seismic loading, 11th European Conf. on Earthquake Engineering (Rotterdam).
[33] Shahrour, I., Benzenati, I., and Khoshravan Azar, A. (1995a). Validation of a nonlinear coupled dynamic model on centrifuge tests of VELACS project, Numerical Models in Geomechanics NUMOG V, (Rotterdam), pp. 269–274.
[34] Shahrour I., Ghorbanbeigi S., and Von Wolffersdorff P.A. (1995b) Comportement des rideaux de palplanche : expérimentation en vraie grandeur et prédictions numériques. Revue Française de Géotechnique, 71, 39-47 (in French).
[35] Shao, C., and Desai, C.S. (2000). Implementation of DSC model and application for analysis of field pile tests under cyclic loading, Int J for Numerical and Analytical Methods in Geomechanics, 24(6), 601–624.
[36] Simpson, B. (1992). Retaining structures : displacement and design, Géotechnique 42(4), 541–576 (https://doi.org/10.1680/geot.1992.42.4.541).
[37] Tatsuoka, F.M., Sakamoto, M., Kawamura, T., and Fakushiima, S. (1986). Strength and deformation characteristics of sand in plane strain compression at extremley low pressures, Soils and Foundations, 26(1), 65–84.
[38] Von Wolffersdorff P.-A. (1994a) Spundwand-Feldversuch in Hochstetten / Sheetpile wall field test in Hochstetten. Part A: Presentation of the problem. Part B: Test results and predictions. Workshop Sheet Pile Test Karlsruhe, Delft University, October 6 and 7, 1994
[39] Von Wolffersdorff P.-A. (1994b) « Results of field test and evaluation of the predictions and subsequent calculations », Workshop Sheet Pile Test Karlsruhe, Delft University.

[40] Zaher, M. (1995). Validation des modèles de sols sur ouvrages types. PhD Thesis, Université des sciences et technologies de Lille.
[41] Zdravkovic, L., Potts, D.M., and St John, H.D. (2005). Modelling of 3D excavation in finite element analysis. Géotechnique 55(7), 497–513 (https://doi.org/10.1680/geot.2005.55.7.497).
[42] Zhang, W., Goh, A.T.C., and Xuan, F. (2015a) A simple prediction model for wall deflection caused by braced excavation in clays, Computers and Geotechnics 63, 67-72. http://dx.doi.org/10.1016/j.compgeo.2014.09.001
[43] Zhang, W., Goh, A.T.C., and Zhang, Y. (2015b) Updating soil parameters using spreadsheet method for predicting wall deflections in braced excavations. Geotechnical and Geological Engineering 33, 1489-1498, DOI 10.1007/s10706-015-9914-4
[44] Zhang, W.G., Goh, A.T.C., Chew, O.Y.S., Zhou, D., and Zhang, R. (2018a) Performance of braced excavation in residual soil with groundwater drawdown, Underground Space 3, 150-165. https://doi.org/10.1016/j.undsp.2018.03.002
[45] Zhang, W., Wang, W., Zhou, D., Zhang, R., Goh, A.T.C., and Hou, Z. (2018b) Influence of groundwater drawdown on excavation responses - A case history in Bukit Timah granitic residual soils. Journal of Rock Mechanics and Geotechnical Engineering 10, 856-864. (https://doi.org/10.1016/j.undsp.2018.03.002)